Ceria-Doped Ni/SBA-16 Catalysts for Dry Reforming of Methane
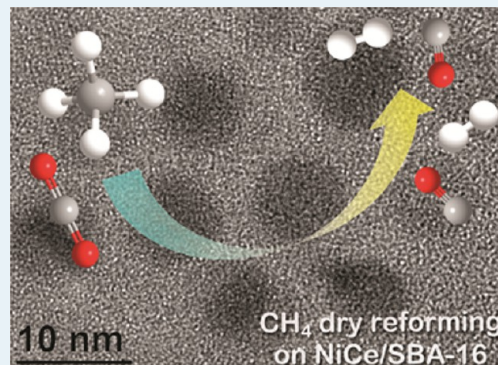
Shenghong Zhang,*,[†] Satoshi Muratsugu,[†,‡] Nozomu Ishiguro,[†] and Mizuki Tada*,[†,‡]

[†]Institute for Molecular Science and [‡]The Graduate University for Advanced Studies (SOKENDAI), 38 Nishigo-naka, Myodaiji, Okazaki, Aichi 444-8585, Japan

S Supporting Information

ABSTRACT: Ni-ceria nanoparticles (Ni/Ce = 1/1) in the cage-like pores of SBA-16 were prepared and evaluated in methane dry reforming reactions. Coexistence of ceria in NiCe/SBA-16 resulted in forming uniformly sized Ni particles (av. 5.7 nm) within the mesopores of SBA-16, because of the confinement effect from the framework of SBA-16 and the strong interaction between Ni and ceria. Ceria addition facilitated the reduction of NiCe/SBA-16 compared with Ni/SBA-16, and Ce^{3+} was the dominant species in both fresh and used NiCe/SBA-16 catalysts, as determined by Ce L_{III}-edge X-ray absorption near-edge structure (XANES). The methane conversion was much more stable on NiCe/SBA-16 than on Ni/CeO_2 and Ni/SBA-16 in the methane dry reforming at 973 K during a 100 h reaction period; the deactivation of the Ni catalyst and the collapse of the SBA-16 framework were preferably suppressed for NiCe/SBA-16 under the reaction conditions. The remarkable effect of ceria on the structural stability of both the active Ni particles and the SBA-16 framework led to the consistent catalytic performance of NiCe/SBA-16 in methane dry reforming.

CH₄ dry reforming on NiCe/SBA-16
10 nm

KEYWORDS: methane dry reforming, nickel catalyst, mesoporous support, SBA-16, ceria, XAFS

INTRODUCTION

Ni-based catalysts with activity and selectivity comparable to those of noble metals but with lower cost have been widely studied in the dry reforming of methane (DRM), which produces syngas with a suitable CO/H_2 ratio (1/1) for downstream industrial processes including Fischer–Tropsch, methanol and dimethyl ether syntheses.[1–3] However, poor stability caused by carbon deposition and aggregation of active Ni metal limits the industrial application of Ni catalysts in DRM reactions. Preventing the deactivation of Ni catalysts still remains a major challenge.

Recently, Ni particles with sizes of several nanometers have proved capable of suppressing the formation of filamentous carbon and its subsequent transformation to the inactive graphite in methane reforming.[4,5] It was suggested that small Ni particles processing a high saturation concentration of carbonaceous species could lower the driving force for carbon diffusion through the Ni crystals,[6] and facilitate the removal of carbon by CO_2 and other oxidants. Inspired by the positive effect of small Ni particles on resistance to carbon deposition, many efforts have been devoted in controlling the sizes of Ni particles, such as dispersing metallic Ni in porous alumina[7–10] and silica.[11–17] These porous oxides have been reported to be generally capable of improving Ni dispersion and suppressing the aggregation of Ni nanoparticles by offering large surface areas and multiple pores. In the case of mesoporous alumina, addition of basic promoters into the framework of alumina[18] is beneficial to reduce the number of strong surface acidic sites, which are responsible for the acceleration of carbon accumulation. In contrast, ordered mesoporous silica, which

is almost neutral, appears to be much more suitable for hosting metal nanoparticles in its mesopores. Specifically, the large surface areas of SBA-15 and MCM-41 allow for high dispersion of Ni metal, and the anchored Ni particles in the silica matrix appear to be stabilized by channels in the silica framework. Improved durability of Ni catalysts in methane reforming has been reported on these supports.[11–17]

However, these two-dimensional hexagonal materials do not sufficiently suppress the aggregation of Ni particles at high temperature. For example, a considerable amount of Ni particles larger than 30 nm, far beyond the pore size of the employed MCM-41 support (2.5 nm), were observed on 2% Ni/MCM-41 catalyst after DRM.[13] The movement of Ni particles within the internal channels or from internal mesopores to the external surface of the mesoporous silica can occur either in reduction of NiO by H_2[19] or under harsh reaction conditions,[13] but the fundamental cause is the inherently weak interaction between Ni particles and the silica matrix, especially at high temperature in the presence of steam. To deal with such conditions, three-dimensional cubic SBA-16 with cage-like mesopores and thick pore walls[20] offers an alternative way to immobilize Ni nanoparticles for DRM. The Ni particles incorporated into SBA-16 pores were smaller than those in SBA-15 under identical preparation conditions, and the Ni particles in SBA-16 were more efficient in the selective hydrodechlorination of 1,1,2-trichloroethane.[21]

Another popular method for stabilizing Ni particles in the nanotubular channels of two-dimensional silica is the introduction of a second metal. The promotion effect of the coexisting noble metals has been widely explored and well summarized recently,[22] but non-noble metals are attracting more and more attention because of their low costs. Incorporation of Zr into Ni-MCM-41 remarkably promoted Ni dispersion and its long-term stability for DRM as a result of the anchoring effect of ZrO_2.[13] A MgO layer coated on silica surface induced strong interaction of Ni species with the support through the formation of NiO-MgO solid solution and Mg_2SiO_4 species, which were thought to prevent the sintering of metallic Ni species.[23] Another noteworthy promoter is CeO_2, since it exhibits excellent low-temperature redox property and the capacity to stabilize the loaded metals resulted from the strong metal–support interaction.[24−26] Recent publications[27,28] have demonstrated that metallic Ni layers formed instead of spherical Ni particles on Ni/CeO_2 catalyst after H_2 reduction at high temperature spread out, and even penetrate into, the partially reduced CeO_x support because of the strong metal–support interaction. In addition, enhanced capacity to provide surface oxygen species to accelerate the removal of deposited carbon should also be responsible for the reported high durability of ceria supported or doped Ni catalysts.[29−34] Recently, the catalytic behavior of Ni/Ce-SBA-15 catalyst in DRM was studied.[34] Ni loaded onto the ceria-coated SBA-15 showed superior stability to that loaded on a bare SBA-15 support. However, a marked decline in CH_4 conversion accompanied by slight growth of Ni particles was still identified with increasing reaction time, probably because of the movement of Ni species in the tubular channels of the support.

In this study, three-dimensional cubic SBA-16 with cage-like mesopores and thick pore walls was used as a support to confine Ni nanoparticles for DRM. Five weight percent Ni/SBA-16 modified with equimolar ceria relative to Ni was prepared, and the structure of the confined ceria-doped Ni catalyst in SBA-16 was characterized by multiple techniques. The effects of ceria on the structural stability and the DRM performances on the NiCe/SBA-16 catalyst were evaluated and interpreted.

■ EXPERIMENTAL SECTION

Catalyst Preparation. SBA-16 was synthesized according to an established method.[20] Typically, 5 g of Pluronic F127 (Aldrich) was dissolved in 250 mL of a 1.6 M HCl aqueous solution. After stirring at 313 K for 1 h, 17.50 g of tetraethoxysilane (TEOS, Wako, 95%) was dropped into the solution. The molar ratio of TEOS/F127/HCl/H_2O was controlled at 1/0.005/5/175. The obtained mixture was vigorously stirred at 313 K for 20 h before hydrothermal treatment at 353 K for 48 h under static conditions. A obtained white precipitate was filtered, washed with water, and dried overnight at 353 K. Finally, the copolymer template F127 was removed by calcination at 823 K for 4 h in a dry air flow (50 mL min^{-1}).

NiCe/SBA-16 catalysts were prepared by incipient wetness impregnation. SBA-16 (1.0 g) was added into an aqueous mixture (1.25 mL) of $Ni(NO_3)_2 \cdot 6H_2O$ (Wako, 99.9%) and $Ce(NO_3)_3 \cdot 6H_2O$ (Wako, 99.9%), and the mass contents of Ni and ceria were controlled at 5% and 14.7%, respectively, with the molar ratio of Ni/Ce equal to 1/1. The mixture was dried in air at 313 K and then heated in a He flow (50 mL min^{-1}) from room temperature to 773 K at a rate of 2 K min^{-1}. Further

isothermal treatment at 773 K was performed for 4 h. The obtained powder was ground and sieved to retain particles with diameters of 180−250 μm for catalytic tests. Five weight percent Ni/SBA-16 was prepared in the absence of $Ce(NO_3)_3 \cdot 6H_2O$ with a similar procedure, and 5 wt % Ni/CeO_2 was prepared using CeO_2 (Aldrich) in a similar way.

Characterization. Nitrogen adsorption isotherms were measured at 77 K using a physisorption analyzer (ASAP 2020, Micromeritics). Samples were outgassed at 473 K for 2 h prior to adsorption measurements. Specific surface area (S_{BET}) was estimated from nitrogen adsorption data in the relative pressure range from 0.05 to 0.20 using the Brunauer−Emmett−Teller (BET) method. Total pore volume (V_t) was estimated from the amount of adsorbed nitrogen at a relative pressure of 0.99.[35] The pore size distribution (PSD) was analyzed by using the nonlocal density functional theory (NLDFT) method[36,37] considering the adsorption branch of the isotherm, which was performed using an Autosorb-1-C software (Quantachrome Inc.). A hybrid model used for the NLDFT evaluation was the adsorption of N_2 at 77 K on silica with cylindrical and spherical geometry for micropores and mesopores, respectively.[36,38] The volume of complementary pores (V_c) including interwall micropores and ordered apertures interconnecting adjacent spherical mesopores[39,40] was calculated by integration of the PSD up to 5 nm, and the volume of primary mesopores (V_p) was estimated by integration of the PSD from 5 to 12 nm. Primary pore diameter (ω_{DFT}) was evaluated at the maximum of the PSD curve.

Powder X-ray diffraction (XRD) patterns were recorded on a Rigaku MultiFlex X-ray diffractometer (Cu Kα, λ = 1.5418 Å, 40 kV, 40 mA). Small-angle XRD patterns were recorded in the range of 0.5−2.5° with a step of 0.01° (2θ) and 10 s for each step. Otherwise, data were collected at a scan rate of 2° min^{-1}. Temperature-programmed reduction with H_2 (H_2-TPR) was performed in a quartz tube (I.D. = 6 mm). Ni catalyst (50 mg) was sandwiched with quartz wool and then reduced by 10% H_2/N_2 (40 mL min^{-1}) with increasing temperature from 293 to 1073 K at a constant rate of 10 K min^{-1}. Change in H_2 concentration in the exit stream was monitored using a thermal conductivity detector (TCD) on a gas chromatograph (Shimadzu GC-8A) after removing water with a liquid N_2 trap. Detector response was calibrated by the reduction of CuO powder (Aldrich) under identical conditions.

Ni dispersions of fresh catalysts were measured by CO chemisorption using a closed vacuum glass line. Typically, 200 mg of a Ni catalyst was reduced in 10% H_2/N_2 at 1073 K for 1 h, and then evacuated at 773 K for 2 h to clean the surface of the sample. After cooling to room temperature under vacuum, CO adsorption was measured in the pressure range of 2.5−12 kPa. Then, the CO-saturated sample was outgassed under 10^{-2} Pa at room temperature for 2 h, and a second adsorption of CO was measured. Differences between the above two adsorption measurements were extracted and extrapolated to estimate the amount of irreversibly adsorbed CO. Ni dispersion was then calculated from the irreversible adsorption of CO assuming the stoichiometric ratio of CO/Ni$_{surface}$ is 0.5.[41]

The morphology of the Ni catalysts was examined by transmission electron microscopy (TEM, JEOL JEM-3200FS) using an accelerating voltage of 300 kV. Raman spectra of deposited carbon on used catalysts were measured on a Renishaw inVia Reflex Raman spectrometer equipped with a Leica microscope and a CCD detector. Raman spectra were collected in the 200−3000 cm^{-1} region by visible laser
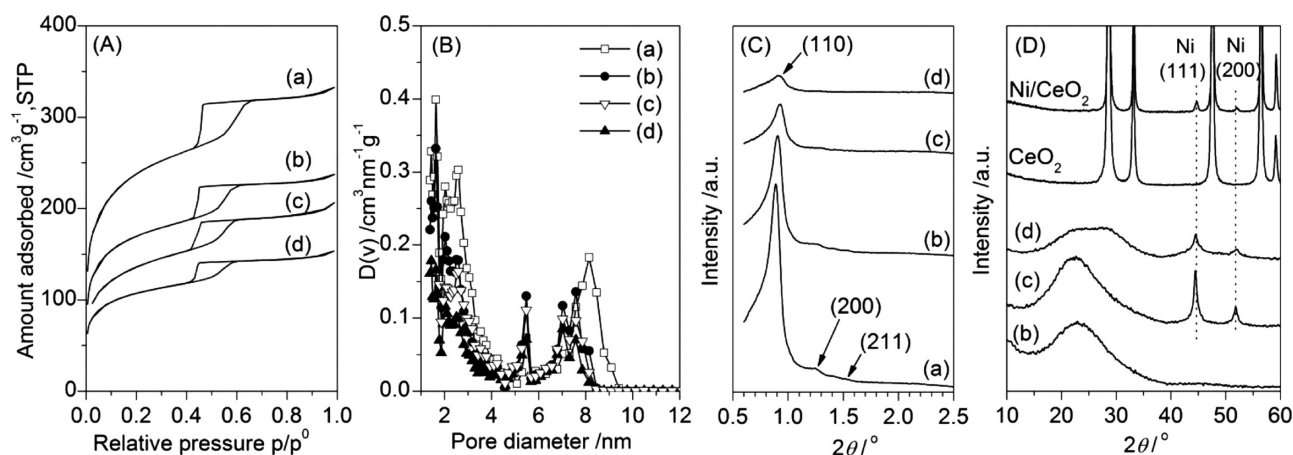
Figure 1. (A) N$_2$ adsorption/desorption isotherms, (B) pore size distributions calibrated using the NLDFT method, (C) small-angle and (D) wide-angle XRD patterns for (a) as-prepared SBA-16 after calcination at 823 K for 4 h, (b) He-treated SBA-16 at 1073 K for 1 h, (c) Ni/SBA-16, and (d) NiCe/SBA-16. Five weight percent Ni was loaded and molar ratio of Ni/Ce was 1/1 in the case of NiCe/SBA-16. All Ni-contained samples were reduced with H$_2$ at 1073 K for 1 h.

excitation at 633 nm. The amount of deposited carbon was quantified by thermogravimetric analysis (TGA) on TGA 2950 (TA Instruments) from room temperature to 1073 K in a dry air flow (40 mL min^{-1}). The reactivity of deposited carbon was investigated by temperature-programmed hydrogenation (TPH). A used Ni catalyst (1.50 mg) was first sandwiched with quartz wool in a tubular quartz reactor (i.d. = 4 mm), and then heated to 1123 K at a rate of 10 K min^{-1} in a 10% H$_2$/N$_2$ flow (20 mL min^{-1}). The production of CH$_4$ was monitored by an online flame ionization detector (FID, Shimadzu GC-2014).

Ni K-edge and Ce L$_{III}$-edge X-ray absorption fine structure (XAFS) were measured at 298 K at the BL-9C station of the Photon Factory at the High Energy Accelerator Research Organization, Japan. The energy and current of electrons in the storage ring were 2.5 GeV and 450 mA, respectively. X-rays from the storage ring were monochromatized by Si(111) double crystals. Ni K-edge XAFS spectra were measured in fluorescence mode, with incident and fluorescent X-rays detected by an ionization chamber filled with N$_2$ and a Lytle detector filled with Ar, respectively. The Ce L$_{III}$-edge X-ray absorption near-edge structure (XANES) was measured in transmission mode, where incident and transmitted X-rays were detected by ionization chambers filled with N$_2$ and N$_2$ (85%) + Ar (15%), respectively. Ni K-edge XANES, extended XAFS (EXAFS), and Ce L$_{III}$-edge XANES spectra were analyzed with IFEFFIT (Athena and Arthemis) ver. 1.2.11.[42,43] Background subtraction was performed with Autobk and Spline smoothing algorithm in the Athena program. k^3-Weighted Ni K-edge EXAFS oscillations (k = 30−130 nm^{-1}) were Fourier transformed into R-space, and EXAFS curve-fitting analysis was carried out in R-space. Fitting parameters were coordination number (CN), interatomic distance (R), Debye−Waller factor (σ^2), and correction-of-edge energy (ΔE_0). Phase shifts and backscattering amplitudes were calculated from the crystal structures of Ni foil and NiO by using the FEFF8 code,[44] and S_0^2 values were determined by their curve-fitting analysis.[45]

Catalytic Reactions. Methane dry reforming was performed under ambient pressure in a tubular quartz reactor (i.d. = 4 mm) with catalysts sandwiched between two quartz wool layers in the heating zone of a furnace. Reaction temperature was controlled by a K-type thermocouple closely attached to

the outside of the catalyst bed and flow rates of CH$_4$ (99.999%), He (99.999%), and CO$_2$ (99.995%) were controlled by mass flow controllers. Typically, catalyst granules (20 mg, 180−250 μm) were diluted with acid-washed quartz sand (Soekawa, 50 mg, 100−200 μm) and pretreated in a 10% H$_2$/N$_2$ flow (20 mL min^{-1}) at 1073 K for 1 h before being cooled to 973 K; then a gas feed (CH$_4$/CO$_2$/He = 1/1/1, 15 mL min^{-1}) was supplied into the reactor. The reaction stream from the outlet was collected with a 100 μL sampling loop and analyzed by an online GC system (Shimadzu GC-8A) equipped with a TCD and a packed column (active carbon, 60−80 mesh (GL Sciences); 3 mm × 3 m) to separate H$_2$, CO, CO$_2$, CH$_4$, and H$_2$O, as described previously.[46]

Conversions and selectivity were defined as

$$X_{CH_4} = \frac{(CH_4)_{in} - (CH_4)_{out}}{(CH_4)_{in}} \times 100\%$$

$$X_{CO_2} = \frac{(CO_2)_{in} - (CO_2)_{out}}{(CO_2)_{in}} \times 100\%$$

$$S_{H_2} = \frac{(H_2)_{out}}{2(CH_4)_{in} \times X_{CH_4}} \times 100\%$$

(CH$_4$)$_{out}$, (CO$_2$)$_{out}$, (CO)$_{out}$, and (H$_2$)$_{out}$ (those in the outlet) were quantified by TCD-GC, while (CH$_4$)$_{in}$ and (CO$_2$)$_{in}$ (those in the inlet) were estimated by the summation of CH$_4$, CO$_2$, and CO in the outlet as follows

$$(CH_4)_{in} = (CO_2)_{in} = \frac{(CH_4)_{out} + (CO_2)_{out} + (CO)_{out}}{2}$$

CH$_4$ turnover rates were measured using pulse reactions in the same reactor. Ni catalyst pellets (5 mg, 106−150 μm) were diluted with quartz sand (50 mg, 100−200 μm) and reduced in H$_2$, as described above, prior to the pulse tests at 973 K. CH$_4$/CO$_2$ pulses (1/1, 883 μL) were injected to the reactor under a He carrier gas flow (50 mL min^{-1}) at an interval of 5 min. CH$_4$ in the exit stream was continuously monitored with an online FID (Shimadzu GC-2014). CH$_4$ conversion of each pulse was calculated by comparing the CH$_4$ peak area of the pulse outflow with that of the blank test using quartz sand without catalysts.
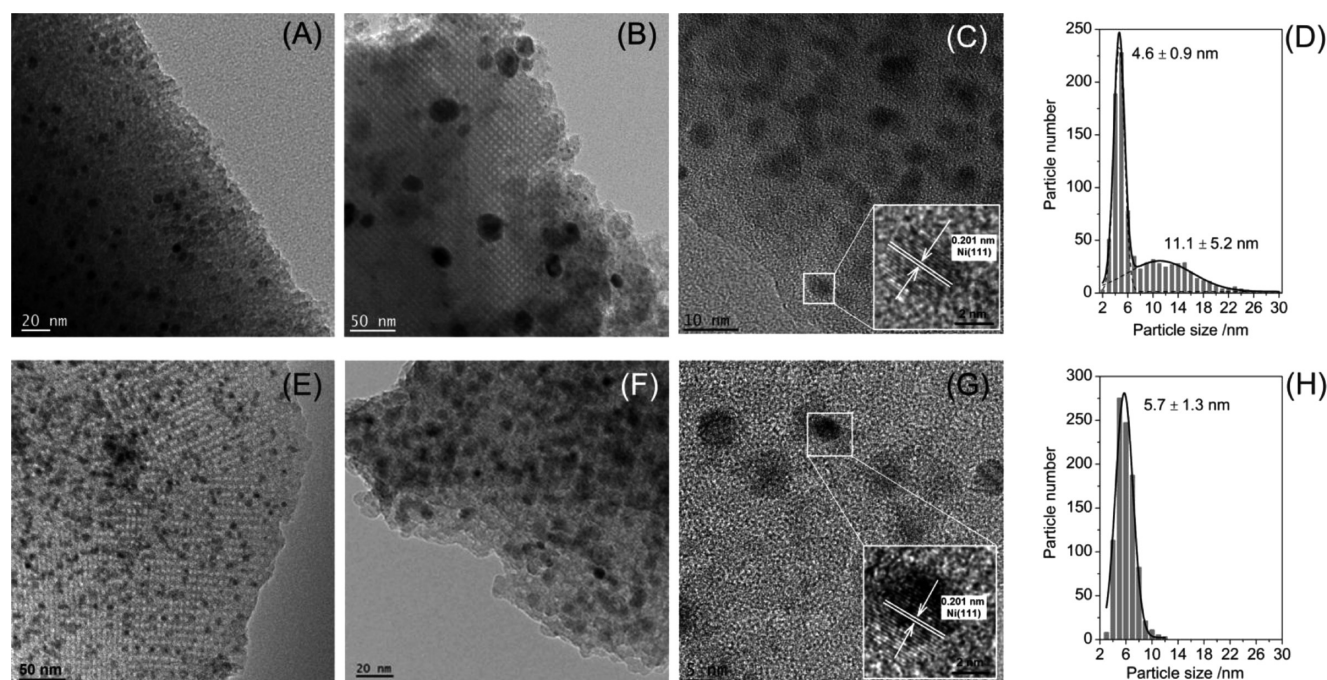
Figure 2. TEM images of (A–C) Ni/SBA-16 and (E–G) NiCe/SBA-16, with Ni particle size distributions for (D) Ni/SBA-16 and (H) NiCe/SBA-16. Five weight percent Ni was loaded, and the molar ratio of Ni/Ce was 1/1 in the NiCe/SBA-16 catalyst. Catalysts were reduced with H_2 at 1073 K for 1 h.

■ RESULTS AND DISSCUSSION

Catalyst Characterization. The textural properties of SBA-16, Ni/SBA-16, and NiCe/SBA-16 were evaluated by N_2 adsorption and small-angle XRD measurements. All samples display type-IV N_2 adsorption/desorption isotherms with a hysteresis loop at relative pressure in the range of 0.45 and 0.6 as shown in Figure 1A. The type-IV isotherms suggest the existence of ink-bottle pores in the above samples.[36] Pore size distribution evaluated from the adsorption branch of the N_2 isotherm by the NLDFT method (Figure 1B) shows the primary mesopores of SBA-16 at the diameter of 8.2 nm, with volume of mesopores and specific surface area estimated to be 0.137 cm³ g⁻¹ and 837 m² g⁻¹, respectively (Supporting Information, Table S1). The small-angle XRD pattern of SBA-16 in Figure 1C exhibits a significant peak at 0.89°. ((110) reflection) and two small peaks at 1.25° ((200) reflection) and 1.54° ((211) reflection), suggesting the existence of ordered mesopores in the as-prepared SBA-16 with body-centered cubic symmetry ($Im3m$).[20] TEM images (Supporting Information, Figure S1) of the prepared SBA-16 also present clearly the cage-like pores along [001] and [111] projections.

After loading Ni and Ce onto SBA-16, decreases in the surface areas and pore volumes were both observed (Figure 1A and Supporting Information, Table S1), suggesting the incorporation of ceria into the pores of SBA-16. As a consequence, the reflection intensity of the low-angle peaks became weaker than that of SBA-16 before loading Ni and Ce. It has been reported that shrinkage of the SBA-16 framework can be caused by thermal treatment at high temperature.[47] Similar shrinkage was suggested to partly occur under the catalyst preparation conditions, but TEM images suggested that the pore structures of SBA-16 remained as shown in Figure 2.

The introduction of equimolar ceria relative to Ni obviously improved Ni dispersion. Ni particles with a much narrower size distribution (average 5.7 nm, which is within the pore size of

the SBA-16 support of 7.2 nm (Figure 1B and Supporting Information, Table S1)) located in the cages of SBA-16, as shown in Figure 2F. It is to be noted that large Ni particles above 10 nm were negligible on NiCe/SBA-16 after H_2 reduction. CO chemisorption results also indicated the increase in Ni dispersion from 10.4% for Ni/SBA-16 to 13.3% for NiCe/SBA-16 (Table 1), consistent with TEM observations.

The positive effect of ceria on controlling the Ni particles seemed to be related to the interaction of Ni–Ce mixed oxide formed after the thermal decomposition of metal nitrate precursors. Coexistence of Ce nitrate indeed prevented the formation of large NiO particles in the thermal decomposition

Table 1. Ni Dispersion (D), Average Ni Particle Size (d), Turnover Frequencies, and Amounts of Carbon Deposition (C%) for Different Ni Catalysts

	Ni/CeO$_2$	Ni/SBA-16	NiCe/SBA-16
D^a /%	5.5	10.4	13.3
d /nm	18.2^b/18.0^c	9.6^b/12.2^c	7.5^b/6.6^c
TOF^d / s⁻¹	12.6^e	28.8	15.7^f
C^g /%	27.8	2.9	3.8

^{a}Ni dispersion was calculated from CO chemisorption results. ^{b}Average Ni particle size was estimated from Ni dispersion using $d = 1/D$,[61] assuming the spherical geometry of Ni particles. ^{c}Average Ni particle size was calculated from TEM observations using the equation $\bar{d} = \sum_i n_i d_i^3 / \sum_i n_i d_i^2$.[62] ^{d}TOF values were calculated from the methane conversion of the first pulse reaction using the ratio of the converted methane to the exposed Ni sites estimated from CO chemisorption $r = (CH_4)_{conv}/Ni_{CO}$. ^{e}TOF value was obtained from the difference in the converted methane numbers between Ni/CeO$_2$ and CeO$_2$ with the similar mass amounts of ceria to exclude roughly the contribution of ceria on the rate of Ni/CeO$_2$ using $r = ((CH_4)_{Ni/CeO2} - (CH_4)_{CeO2})/Ni_{CO}$, (Supporting Information, Figure S6B). ^{g}C% is the weight percent of deposited carbon on the used Ni catalysts after DRM reactions at 973 K for 100 h.

process of Ni nitrate, in contrast to the case without Ce nitrate (Supporting Information, Figure S2). Reflection peaks corresponding to the NiO phase were obvious in the XRD patterns of NiO/SBA-16, but they were negligible on NiCeO/SBA-16, suggesting the formation of much smaller NiO particles in the presence of Ce. Biphasic mixtures of NiO and CeO_2 have been widely reported under similar conditions.[31,48,49] Indeed, very broad reflection peaks corresponding to CeO_2 were observed on $NiCeO_x$/SBA-16 (Supporting Information, Figure S2), in accordance with its TEM images which showed the lattice of CeO_2 (Supporting Information, Figure S3). However, neither CeO_2 nor Ce_2O_3 crystallites were identified by TEM on the reduced NiCe/SBA-16 sample, even after being treated with a NaOH solution (Supporting Information, Figure S4).

The valence state of Ce in the fresh NiCe/SBA-16 catalyst was examined by Ce L_{III}-edge XANES. Two XANES peaks at 5731.1 and 5738.0 eV corresponding to $2p \rightarrow 4f^1 5d^1 L$ and $2p \rightarrow 4f^0 5d^1$ transitions,[50] respectively, were observed at Ce L_{III}-edge of CeO_2 with Ce^{4+}, whereas a single peak at 5726.6 eV assigned to $2p \rightarrow 4f^1 5d^1$ transition[51] was obtained for $CeCl_3 \cdot 7H_2O$ with Ce^{3+}, (Figure 3A). The fresh NiCe/SBA-16
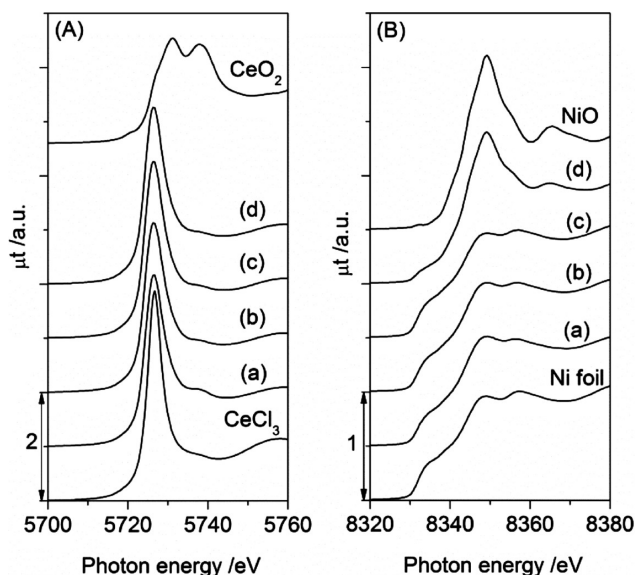

Figure 3. (A) Ce L_{III}-edge and (B) Ni K-edge XANES spectra of (a) fresh NiCe/SBA-16, (b) used NiCe/SBA-16 after DRM at 973 K for 100 h, (c) CH_4-treated NiCe/SBA-16 in 20% CH_4/He (40 mL min^{-1}) for 2 h at 973 K, and (d) CO_2-treated NiCe/SBA-16 in 20% CO_2/He (40 mL min^{-1}) for 2 h at 973 K.

catalyst exhibited a typical characteristic of Ce^{3+} with a sharp peak at 5726.5 eV. This indicated that Ce^{3+} was the dominant species in the fresh NiCe/SBA-16 catalyst.

Figure 3B presents the Ni K-edge XANES spectra, and the fresh NiCe/SBA-16 catalyst produced a XANES spectrum similar to that of Ni foil, indicating the Ni species on the catalyst was metallic. Their k^3-weighted EXAFS Fourier transforms are presented in Figure 4, with curve-fitting results in Supporting Information, Figure S5 and Table S2. The curve-fitting analysis for the fresh NiCe/SBA-16 catalyst suggested that there were Ni−Ni bonds at 0.248 ± 0.001 nm, which was similar to that of Ni foil, with the CN of 10.0 ± 0.9.

Despite the similar CNs of Ni−Ni bonds (Supporting Information, Table S2) evaluated for Ni/SBA-16 (10.0 ± 0.7)
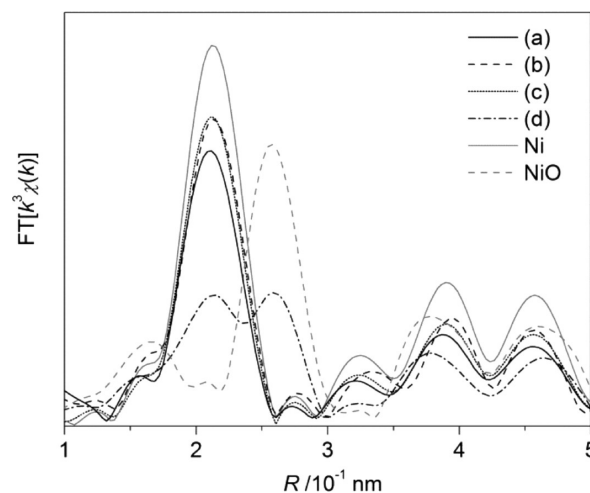

Figure 4. k^3-Weighted Ni K-edge EXAFS Fourier transforms ($k = 30-130$ nm^{-1}) of NiCe/SBA-16, with Ni foil and NiO as references. (a) Fresh NiCe/SBA-16, (b) used NiCe/SBA-16 after DRM at 973 K for 100 h, (c) CH_4-treated NiCe/SBA-16 in 20% CH_4/He (40 mL min^{-1}) for 2 h at 973 K, and (d) CO_2-treated NiCe/SBA-16 in 20% CO_2/He (40 mL min^{-1}) for 2 h at 973 K.

and NiCe/SBA-16 (10.0 ± 0.9), the higher dispersion of Ni species on NiCe/SBA-16 was confirmed by TEM observation and CO chemisorption. It has been reported[27,28] that strong interaction between Ni and ceria flattened the shape of the Ni particles under reduction conditions; the spreading trend of Ni at the interface with ceria would contribute to Ni dispersion after reduction at high temperature. In the case of NiCe/SBA-16, amorphous ceria was supposed to play a key role in regulating Ni dispersion during the reduction process via interaction between Ni and ceria and preferable affinity of cerium oxide toward silica matrix.[52]

The reduction behaviors of Ni catalysts were examined by H_2-TPR (Figure 5). Three H_2 consumption peaks appeared at 504, 583, and 1024 K for Ni/CeO_2. The first peak was attributed to the reduction of adsorbed oxygen species on the vacancy sites generated by the incorporation of Ni^{2+} ions into ceria lattice; the second peak was assigned to the reduction of NiO particles; and the third peak arose from the reduction of
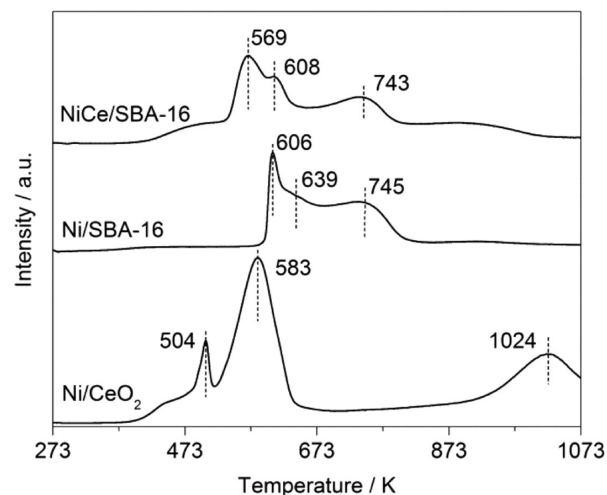

Figure 5. H_2-TPR profiles of Ni/CeO_2, Ni/SBA-16, and NiCe/SBA-16.

bulk ceria.[48] For Ni/SBA-16, a sharp peak at 606 K and a broad one with a maximum at 745 K were observed, along with a shoulder peak at 639 K. The sharp peak and the shoulder one were caused by the reduction of NiO crystallites with weak interaction toward silica support, while the broad peak at the higher temperature was due to the reduction of NiO species dispersed on the silica support, which were likely Ni hydrosilicate species.[53]

Similar to Ni/SBA-16, three reduction peaks appeared at 569, 608, and 743 K on NiCe/SBA-16, attributed to the reduction of Ni–Ce biphasic oxides and dispersed Ni hydrosilicates, respectively. The calculated reducibility of Ni from the TPR profiles is presented in Supporting Information, Table S3, which suggested that the mass of the Ni species were reduced. Compared with Ni/SBA-16, the introduction of CeO_2 decreased the reduction temperature of NiO, which was even lower than that of the NiO phase in Ni/CeO_2. The incorporation of Ni^{2+} into ceria lattice after the thermal decomposition of NiCe/SBA-16 catalyst led to the formation of Ni–Ce–O species and the enhancement of the lattice distortion of ceria,[31,48,49] which were responsible for the facilitated reduction behavior of NiCe/SBA-16. However, appearance of the peak at 743 K assigned to the reduction of Ni hydrosilicates indicated that a part of the Ni species were not incorporated into the Ni–Ce–O oxides, suggesting two kinds of Ni species in the NiCe/SBA-16 catalyst.

Together with the N_2 physisorption, XRD, XAFS, TEM, and H_2-TPR results, it can be inferred that reduced ceria likely dispersed onto the surface of SBA-16. This is consistent with the previous report[54] that ceria has strong affinity toward mesoporous silica and some Ce species with tetrahedral environment dispersed on a silica surface. The dispersed ceria with Ce^{3+} was suggested to act as a barrier layer to prevent the intimate contact of Ni and silica because of the strong interaction between Ni and ceria.

Catalytic Performance. Catalytic rates were measured from CH_4/CO_2 (1/1) pulse reactions at 973 K with a short reactor residence time and low CH_4 conversions (<40%, much lower than CH_4 equilibrium conversion (89%) at 973 K) to keep the reaction far from thermodynamic equilibrium. Under such conditions, effluence from the reverse reaction on the CH_4 turnover rates can be significantly reduced.[55,56]

Catalytic rates were normalized to the exposed Ni sites which were determined by the CO chemisorption. Measured CH_4 turnover frequency (TOF) for each pulse reaction is presented in Supporting Information, Figure S6A, and the rate for the first pulse reaction was referred to as the initial CH_4 conversion rate in Table 1. The measured initial rates for Ni/CeO_2, Ni/SBA-16, and NiCe/SBA-16 were 12.6, 28.8, and 15.7 s^{-1}, respectively, regardless of the effect of the doped ceria on the activity of NiCe/SBA-16. Recently, the intrinsic activity of Ni/SiO_2 catalysts for DRM was reported to be independent of the average Ni particle size.[57] The calculated lowest value of Ni/CeO_2 was suggested to be a result of the SMSI effect between Ni and ceria.[58] Addition of 15% ceria into Ni/SBA-16 decreased the initial methane reforming activity significantly, which was consistent with the reported negative effect of ceria on the methane reforming activity of Ni metal when ceria mass content was above 10%.[59,60]

The stabilities of the Ni catalysts were examined during a 100 h DRM reaction period at 973 K (Figure 6). The identical initial methane conversions on the three catalysts were not suitable to compare differences in the catalytic rates on the
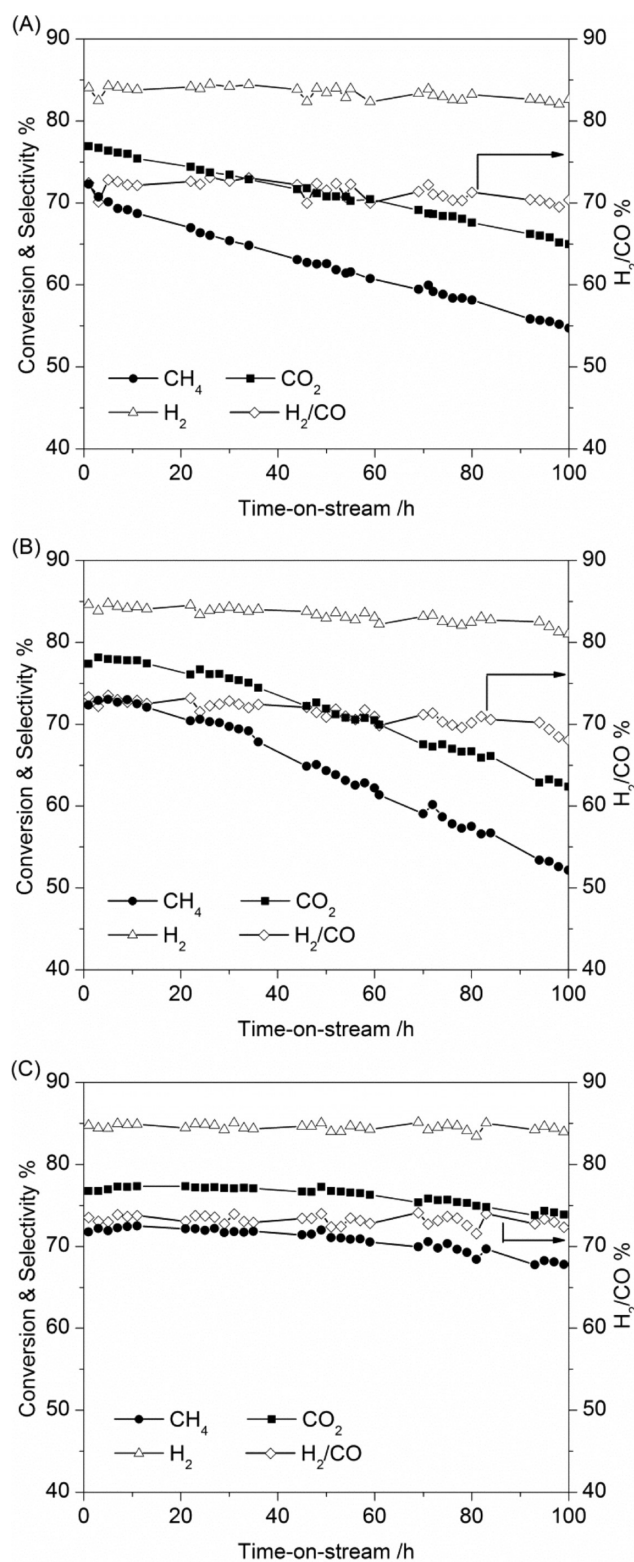

Figure 6. Dependence of catalytic performance of (A) Ni/CeO_2, (B) Ni/SBA-16, and (C) NiCe/SBA-16 on reaction time (conditions: 20 mg of Ni catalyst, 973 K, $CH_4/CO_2/He$ = 5/5/5, total flow = 15 mL min^{-1}).

three catalysts since the reaction data were recorded under the quasi-equilibrium reaction conditions with a low space velocity. However, a significant decline in the CH_4 conversions from 73 to 52% and 72 to 55% were observed on Ni/SBA-16 and Ni/

CeO_2, respectively. Whereas NiCe/SBA-16 exhibited superior stability, with a slight decrease in the CH_4 conversion from 72 to 68% observed during the 100 h reaction period. In contrast, Ni loaded on MCM-41 with thinner pore walls suffered much more serious deactivation, with a drop in methane conversion from 75 to 57% in a 50 h reaction under the similar conditions.[13] Ni/Ce-SBA-15 with tubular channels also exhibited the inferior stability to NiCe/SBA-16, with methane conversion decreasing from 77 to 72% after 50 h reaction.[34] Thus, the Ni catalyst supported on SBA-16 with ceria was found to be superior in the DRM performance under the identical reaction conditions.

Differences in the catalyst deactivation between Ni/SBA-16 and NiCe/SBA-16 were consistent to the results of the pulse reaction tests (Supporting Information, Figure S6A). Continuous decrease in the methane turnover rates was observed on Ni/SBA-16 as the pulse number increased, in spite of its highest initial methane conversion rates. On the other hand, the activity of NiCe/SBA-16 initially decreased, but it became stable after several pulses. Even evaluated in the pure CH_4/CO_2 stream without the He carrier, the deactivation of NiCe/SBA-16 was significantly suppressed compared to that on Ni/SBA-16 (Figure 6 and Supporting Information, Figure S7). The observed degradation in the catalytic performances of Ni/CeO_2 and Ni/SBA-16 after long operation time was suggested to be caused by the carbon accumulation and the structural decomposition of SBA-16 as discussed below.

Carbon accumulation has been a critical issue for the degradation of CH_4 reforming catalysts.[63] There are two general pathways to produce carbon deposition in CH_4 reforming reactions: CH_4 decomposition ($CH_4 \rightarrow C + 2H_2$) and CO disproportionation ($2CO \rightarrow C + CO_2$, the Boudouard reaction).[63] The latter was confirmed to be the dominant carbon formation mechanism on Ni catalysts for DRM.[64] The diffusion of carbon through a metal particle results in forming filamentous whisker carbon, carbon nanotubes, and shell-like graphite.[65,66] The deposited carbon can be readily gasified by steam at high temperature ($C + H_2O \rightarrow CO + H_2$), but the carbon gasification by reactive CO_2 is relatively slow for DRM, where easier carbon gasification by steam is greatly suppressed by the limited formation of water as a byproduct.

XRD patterns of the used Ni catalysts are presented in Supporting Information, Figure S8. In addition to the characteristic peaks of Ni metal at 2θ of 44.5° and 51.9°, a broad peak at 2θ of 26.0° was assigned to the reflection from the (111) plane of graphite formed on active Ni metal.[67] The strong intensity of this peak for the used Ni/CeO_2 suggests the significant deposition of graphitic carbon on Ni/CeO_2 after the long-term DRM reaction. A similar peak with lower intensity was also observed on the used Ni/SBA-16 catalyst (Supporting Information, Figure S8). In contrast, this peak was invisible on the used NiCe/SBA-16, suggesting minor graphitic carbon on NiCe/SBA-16.

Raman spectra elucidate more information on the nature of carbonaceous deposits on the used Ni catalysts.[68] Figure 7 displays the Raman spectra of the used catalysts, and four major peaks at 1324 cm^{-1} (D band), 1576 cm^{-1} (G band), 1604 cm^{-1} (D′ band), and 2649 cm^{-1} (G′ band) were observed on all of the used Ni catalysts. The D band is the disorder-induced band, arising from the breathing modes of sp^2 atoms in rings; the G band is attributed to the in-plane C−C stretching vibrations of all pairs of sp^2 atoms in graphite layers; the D′ band, a shoulder peak in G band, is also associated to the presence of defects in
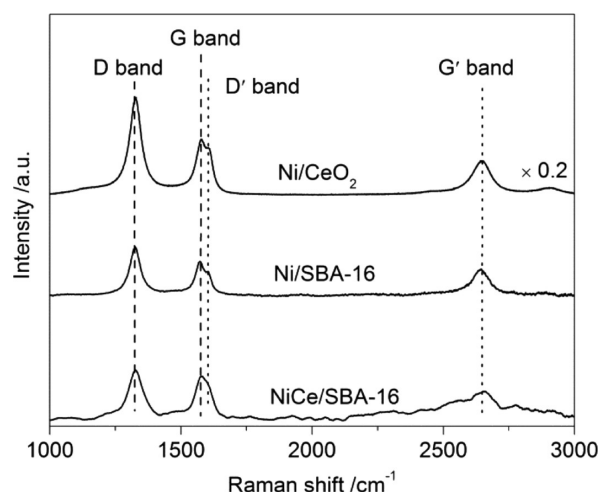

Figure 7. Raman spectra of the used Ni catalysts after DRM at 973 K for 100 h.

graphite and other carbonaceous species; however, the G′ band appearing at approximately twice the frequency of the D band as its second harmonic is independent of lattice defects.[69] The observed relatively strong intensity of the D band to the G band suggests the presence of more disordered carbonaceous species than graphitic carbon on all the used Ni catalysts, since the intensity of the D band increases with the increasing structural imperfections of graphite.[70]

Further quantification of the deposited carbon by TGA (Table 1 and Supporting Information, Figure S9) showed that there were 27.8%, 2.9%, and 3.8% weight percent carbon on the used Ni/CeO_2, Ni/SBA-16, and NiCe/SBA-16, respectively. The highest carbon percent on the used Ni/CeO_2 agreed with the strong signals of graphitic carbon observed on the both XRD and Raman spectra. The reactivity of carbon deposits on Ni/CeO_2 was further examined by TPH experiments (Figure 8). Three types of carbonaceous species classified as polymeric, filamentous, and graphitic carbon (designated as C_α, C_β, and C_γ,[71] respectively) have been reported on the used Ni/CeO_2. The onset temperature of the TPH curves around 473 K could be attributed to the hydrogenation of amorphous polymeric C_α species. The active C_α species is presumed to result from
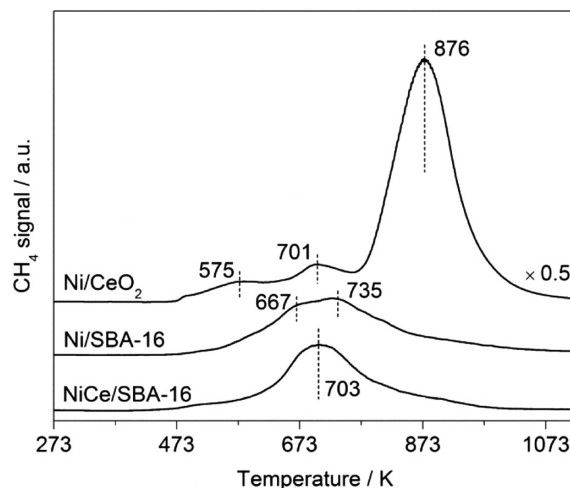

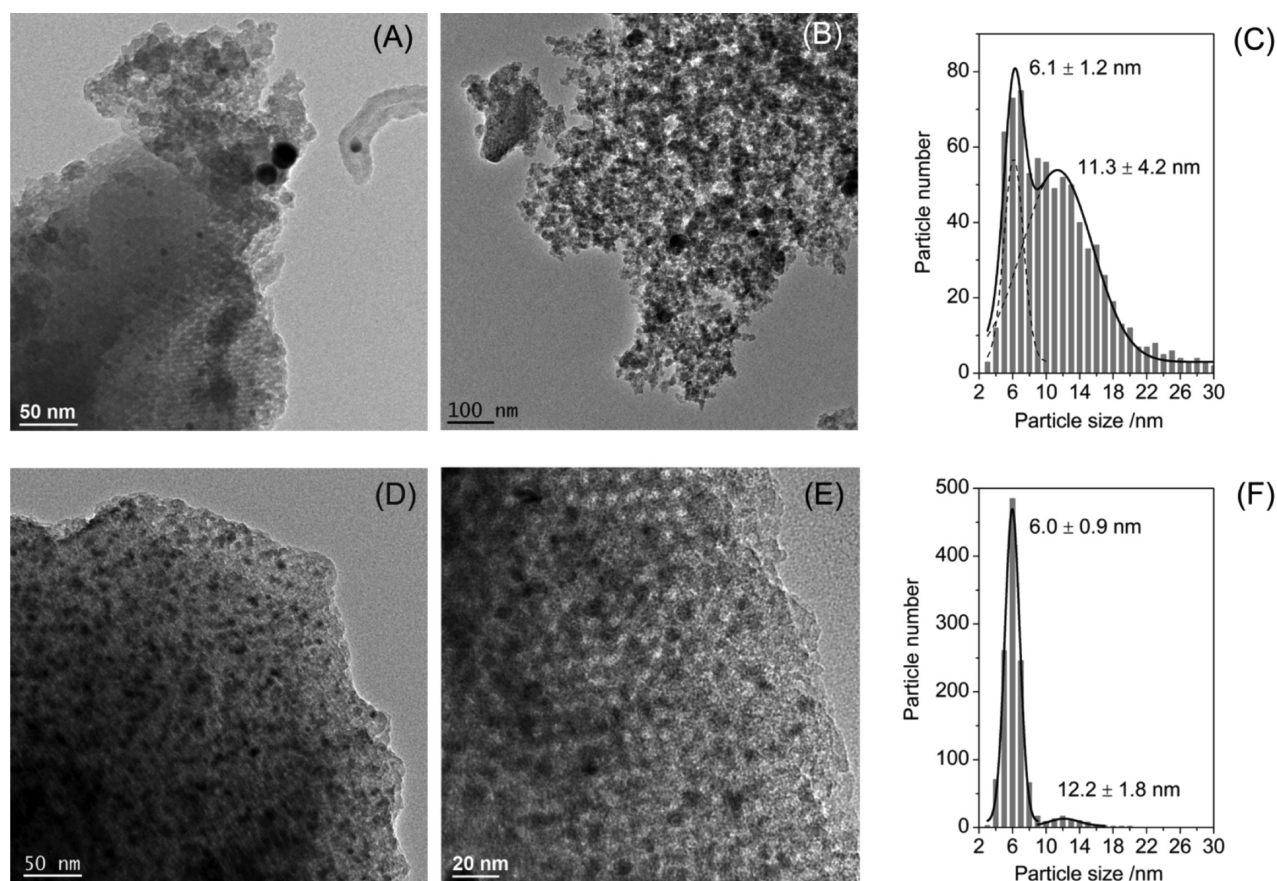**Figure 8.** TPH curves of the used Ni catalysts after DRM at 973 K for 100 h.

Figure 9. TEM images of (A, B) used Ni/SBA-16 and (D, E) used NiCe/SBA-16 after catalytic reactions at 973 K for 100 h, with Ni particle size distributions for (C) used Ni/SBA-16 and (F) used NiCe/SBA-16 catalysts.

thermal decomposition of methane, and considered as important intermediates for the formation of CO, because it can be completely hydrogenated at low temperature.[72] The CH_4 peak appearing at 623–773 K was assigned to the hydrogenation of filamentous C_β species; the dominant peak at 876 K could be regarded as graphitic C_γ species with the lowest reactivity, and appearance of such species would be the main cause for the significant deactivation of Ni/CeO_2.

The reactivities of the deposited carbonaceous species on Ni/SBA-16 and NiCe/SBA-16 were different from each other. Filamentous C_β species dominated on both used catalysts (Figure 8), but the maximum hydrogenation temperature of the C_β species was lower on NiCe/SBA-16 (703 K) than on Ni/SBA-16 (735 K), suggesting the higher reactivity of the C_β species on NiCe/SBA-16 than that on Ni/SBA-16. In addition to the inferior amount of the deposited carbon on NiCe/SBA-16 to Ni/CeO_2, these results would relate to the stable DRM performances on NiCe/SBA-16.

The sintering of Ni particles would be another factor for the decreases in the catalytic DRM performance of Ni/SBA-16. Inherently, weak interaction between Ni and the silica support reduces the stability of Ni particles at high temperature. In the case of Ni/SBA-16, the migration of Ni species from the internal mesopores of SBA-16 to the external surface of the carrier at high temperature caused the aggregation of the Ni particles,[19] and the structural collapse of the mesoporous silica also accelerated the sintering of the Ni particles under the reaction conditions. The TEM images of the used Ni/SBA-16 (Figures 9A and B) showed the partial decomposition of the

ordered SBA-16 framework after the long-term DRM test at 973 K, similar to previously reported Ni catalysts supported on SBA-15[73] and MCM-41.[13] The local collapse of the SBA-16 carrier led to inevitable aggregation of the loaded Ni metal (Figure 9B): small Ni particles with the diameters of 5–8 nm and considerably larger Ni particles of 10–30 nm were observed. A wide distribution of the Ni particle size was obtained as a result (Figure 9C, Supporting Information, Table S4).

The hydrolysis of surface Si–O–Si bonds was reported to be a major reason for the structural degradation of mesoporous silica.[74,75] The structural collapse of Ni/SBA-16 is probably caused by the hydrolysis and rearrangement of surface Si–O–Si bonds, since the formation of steam is unavoidable under the DRM conditions. It was reported that the surface hydroxyl groups of a catalyst support are significantly involved in the hydrolysis of steam and the subsequent oxygen transfer to deposited carbon in the gasification processes of coke.[76] Indeed, Figures 9A and 9B showed the changes in the morphology of the sample after the long reaction for 100 h, and thus the hydrolysis of the surface Si–O–Si bonds on Ni/SBA-16 would be facilitated under steam-rich reaction conditions.

The addition of ceria remarkably enhanced the durability of NiCe/SBA-16 in DRM. The positive effects of ceria on the durability and coke resistance of Ni catalysts were also reported on Ce-doped Ni/Mg–Al,[33] Ni/α-Al_2O_3,[77] and Ni/Ce-SBA-15.[34] It has been suggested that the positive effects have been generally achieved by the excellent redox properties of ceria, which easily releases lattice oxygen under reducing conditions

to create anionic vacancies correlated to high lattice oxygen mobility.[78]

The observed superior stability of NiCe/SBA-16 seemed to be related to the beneficial effect of Ce on the structural stability of both SBA-16 matrix and active Ni species, as well as the facilitated reducibility (Figure 5). Ce L_{III}-edge XANES analysis (Figure 3A) revealed that the Ce^{3+} species was major in the used NiCe/SBA-16 catalyst. The Ce^{3+} species reserved in NiCe/SBA-16 even after being treated with a CO_2/He flow at 973 K for 2 h, indicating that Ce^{3+} was highly resistant to CO_2 at the reaction temperature. There were no significant peaks attributed to crystalline Ce_2O_3 in the XRD patterns of the used NiCe/SBA-16 (Supporting Information, Figure S7), suggesting the existence of amorphous ceria. The amorphous ceria on silica was reported[54] to be capable of producing surface Si−O−Ce bonds with much higher steam resistance than Si−O−Si bonds. This would suppress the attack of Si−O−Si bonds by steam under the DRM reaction conditions, leading to a relatively high hydrothermal stability of NiCe/SBA-16.

The strong interaction between Ni and ceria and confinement effect from the mesocages of SBA-16 suppressed effectively the aggregation of Ni particles for NiCe/SBA-16 catalyst. TEM images of the used NiCe/SBA-16 (Figures 9D and E) showed the ordered structure of SBA-16 with small Ni particles confined in the cages, whose average particle size (6.0 nm) is plotted in Figure 9F. The similarity of the particle size to that of the fresh NiCe/SBA-16 (5.7 nm) suggested the stability of Ce-doped Ni particles in DRM. Ni K-edge XANES and EXAFS suggested that the metallic Ni species were retained in NiCe/SBA-16 after the durability test at 973 K for 100 h. In contrast, the exposure of NiCe/SBA-16 to CO_2 at 973 K for 2 h led to the partial oxidation of Ni (Figure 3B), though Ce^{3+} was not oxidized by CO_2. Curve-fitting analysis suggested that there were Ni−Ni bonds at 0.248 ± 0.001 nm (CN = 4.6 ± 1.4) attributed to Ni metal, Ni−O bonds at 0.210 ± 0.003 nm (CN = 4.6 ± 1.5), and Ni−Ni bonds at 0.296 ± 0.001 nm (CN = 7.2 ± 1.3) assigned to NiO (Figure 4 and Supporting Information, Figure S5 and Table S2). Under steady-state DRM conditions in the presence of CH_4, Ni existed as metallic particles, which would be the active species for DRM. These results also suggested that oxidative deactivation of metallic Ni by CO_2 was effectively inhibited under reaction conditions on the NiCe/SBA-16 catalyst.

CONCLUSIONS

Biphasic Ni−Ce catalyst on SBA-16 has been successfully prepared and evaluated in methane dry reforming. Compared with Ni/SBA-16 without ceria, the incorporation of Ce inhibited effectively the formation of large Ni particles, leading to a uniform distribution of Ni particles (5.7 nm). The strong interaction between Ni particles and ceria and the confinement effect from mesocages of SBA-16 are suggested to contribute to the formation of uniformly sized Ni particles in NiCe/SBA-16.

The NiCe/SBA-16 catalyst exhibited desirable reducibility and stability for methane dry reforming. Ceria with Ce^{3+} in the working NiCe/SBA-16 catalyst suppressed the structural collapse of the SBA-16 framework and consequent Ni sintering under the DRM conditions. Strong interaction between Ni and ceria would not only restrict Ni growth but also reduce the intimate contact of Ni metal and silica surface to decrease the reaction-induced collapse of SBA-16 framework. In addition, the reactivity of the deposited carbon on Ni metal was improved by the accompanied Ce promoters in NiCe/SBA-16.

ASSOCIATED CONTENT

Ⓢ Supporting Information

Detail information on TEM, analysis of N_2 physisorption data, XRD, EXAFS, pulse reactions, and TGA plots. This material is available free of charge via the Internet at http://pubs.acs.org.

AUTHOR INFORMATION

Corresponding Author
*E-mail: mtada@ims.ac.jp (M.T.).

Notes
The authors declare no competing financial interest.

ACKNOWLEDGMENTS

REFERENCES

(1) Bradford, M. C. J.; Vannice, M. A.; Ruckenstein, E. *Catal. Rev. Sci. Eng.* **1999**, *41*, 1−42.

(2) Hu, Y.; Ruckenstein, E. *Catal. Rev. Sci. Eng.* **2002**, *44*, 423−453.

(3) Rostrup-Nielsen, J. R.; Sehested, J.; Norskov, J. K. *Adv. Catal.* **2002**, *47*, 65−139.

(4) Kim, J. H.; Suh, D. J.; Park, T. J.; Kim, K. L. *Appl. Catal., A* **2000**, *197*, 191−200.

(5) Bengaard, H. S.; Nørskov, J. K.; Sehested, J.; Clausen, B. S.; Nielsen, L. P.; Molenbroek, A. M.; Rostrup-Nielsen, J. R. *J. Catal.* **2002**, *209*, 365−384.

(6) Chen, D.; Christensen, K. O.; Ochoa-Fernández, E.; Yu, Z.; Tøtdal, B.; Latorre, N.; Monzón, A.; Holmen, A. *J. Catal.* **2005**, *229*, 82−96.

(7) Fajardo, H. V.; Martins, A. O.; de Almeida, R. M.; Noda, L. K.; Probst, L. F. D.; Carreno, N. L. V.; Valentini, A. *Mater. Lett.* **2005**, *59*, 3963−3967.

(8) Shen, W. H.; Momoi, H.; Komatsubara, K.; Saito, T.; Yoshida, A.; Naito, S. *Catal. Today* **2011**, *171*, 150−155.

(9) Xu, L.; Zhao, H.; Song, H.; Chou, L. *Int. J. Hydrogen Energy* **2012**, *37*, 7497−7511.

(10) Newnham, J.; Mantri, K.; Amin, M. H.; Tardio, J.; Bhargava, S. K. *Int. J. Hydrogen Energy* **2012**, *37*, 1454−1464.

(11) Takahashi, R.; Sato, S.; Sodesawa, T.; Tomiyama, S. *Appl. Catal., A* **2005**, *286*, 142−147.

(12) Zhang, M.; Ji, S.; Hu, L.; Yin, F.; Li, C.; Liu, H. *Chin. J. Catal.* **2006**, *27*, 777−782.

(13) Liu, D.; Quek, X. Y.; Cheo, W. N. E.; Lau, R.; Borgna, A.; Yang, Y. *J. Catal.* **2009**, *266*, 380−390.

(14) Liu, D.; Lau, R.; Borgna, A.; Yang, Y. *Appl. Catal., A* **2009**, *358*, 110−118.

(15) Liu, Z.; Zhou, J.; Cao, K.; Yang, W.; Gao, H.; Wang, Y.; Li, H. *Appl. Catal., B* **2012**, *125*, 324−330.

(16) Quek, X. Y.; Liu, D.; Cheo, W. N. E.; Wang, H.; Chen, Y.; Yang, Y. *Appl. Catal., B* **2010**, *95*, 374−382.

(17) Li, L.; He, S.; Song, Y.; Zhao, J.; Ji, W.; Au, C.-T. *J. Catal.* **2012**, *288*, 54−64.

(18) Xu, L.; Song, H.; Chou, L. *Appl. Catal., B* **2011**, *108−109*, 177−190.

(19) Kantorovich, D.; Haviv, L.; Vradman, L.; Landau, M. V. *Stud. Surf. Sci. Catal.* **2005**, *156*, 147−154.

(20) Zhao, D.; Huo, Q.; Feng, J.; Chmelka, B. F.; Stucky, G. D. *J. Am. Chem. Soc.* **1998**, *120*, 6024−6036.

(21) Park, Y.; Kang, T.; Lee, J.; Kim, P.; Kim, H.; Yi. *J. Catal. Today* **2004**, *97*, 195−203.

(22) Li, D.; Nakagawa, Y.; Tomishige, K. *Appl. Catal., A* **2011**, *408*, 1−24.

(23) Zhu, J.; Peng, X.; Yao, L.; Tong, D.; Hu, C. *Catal. Sci. Technol.* **2012**, *2*, 529−537.

(24) Trovarelli, A.; Deleitenburg, C.; Dolcetti, G.; Lorca, J. L. *J. Catal.* **1995**, *151*, 111−124.

(25) Mogensen, M.; Sammes, N. M.; Tompsett, G. A. *Solid State Ionics* **2000**, *129*, 63−94.

(26) Beckers, J.; Rothenberg, G. *Green Chem.* **2010**, *12*, 939−948.

(27) Gonzalez-DelaCruz, V. M.; Holgado, J. P.; Pereñíguez, R.; Caballero, A. *J. Catal.* **2008**, *257*, 307−314.

(28) Caballero, A.; Holgado, J. P.; Gonzalez-de la Cruz, V. M.; Habas, S. E.; Herranz, T.; Salmeron, M. *Chem. Commun.* **2010**, *46*, 1097−1099.

(29) Kouachi, K.; Menad, S.; Tazkrit, S.; Cherifi, O. *Stud. Surf. Sci. Catal.* **2001**, *138*, 405−412.

(30) Xu, S.; Yan, X.; Wang, X. *Fuel* **2006**, *85*, 2243−2247.

(31) Kim, D. K.; Stoewe, K.; Mueller, F.; Maier, W. F. *J. Catal.* **2007**, *247*, 101−111.

(32) Kumar, P.; Sun, Y.; Idem, R. O. *Energy Fuels* **2007**, *21*, 3113−3123.

(33) Daza, C. E.; Gallego, J.; Mondragon, F.; Moreno, S.; Molina, R. *Fuels* **2010**, *89*, 592−603.

(34) Wang, N.; Chu, W.; Zhang, T.; Zhao, X. *Int. J. Hydrogen Energy* **2012**, *37*, 19−30.

(35) Sing, K. S. W. *Pure Appl. Chem.* **1985**, *57*, 603−619.

(36) Ravikovitch, P. I.; Neimark, A. V. *Langmuir* **2002**, *18*, 1550−1560.

(37) Ravikovitch, P. I.; Neimark, A. V. *Langmuir* **2002**, *18*, 9830−9837.

(38) Thommes, M.; Smarsly, B.; Groenewolt, M.; Ravikovitch, P. I.; Neimark, A. V. *Langmuir* **2006**, *22*, 756−764.

(39) Morishige, K.; Tateishi, N.; Fukuma, S. *J. Phys. Chem. B* **2003**, *107*, 5177−5181.

(40) Grudzien, R. M.; Grabicka, B. E.; Jaroniec, M. *Appl. Surf. Sci.* **2007**, *253*, 5660−5665.

(41) Stuckless, J. T.; Al-Sarraf, N.; Wartnaby, C.; King, D. A. *J. Chem. Phys.* **1993**, *99*, 2202−2212.

(42) Newville, M. *J. Synchrotron Rad.* **2001**, *8*, 322−324.

(43) Ravel, B.; Newville, M. *J. Synchrotron Rad.* **2005**, *12*, 537−541.

(44) Rehr, J. J.; Albers, R. C. *Rev. Mod. Phys.* **2000**, *72*, 621−654.

(45) Chen, Y.; Shen, J.; Chen, N. *Solid State Commun.* **2009**, *149*, 121−125.

(46) Zhang, S.; Muratsugu, S.; Ishiguro, N.; Ohkoshi, S.; Tada, M. *ChemCatChem* **2012**, *4*, 1783−1790.

(47) Kruk, M.; Hui, C. M. *J. Am. Chem. Soc.* **2008**, *130*, 1528−1529.

(48) Shan, W.; Luo, M.; Ying, P.; Shen, W.; Li, C. *Appl. Catal., A* **2003**, *246*, 1−9.

(49) Barrio, L.; Kubacka, A.; Zhou, G.; Estrella, M.; Martinez-Arias, A.; Hanson, J. C.; Fernandez-Garcia, M.; Rodrigues, J. A. *J. Phys. Chem. B* **2010**, *114*, 12689−12697.

(50) Soldatov, A. V.; Ivanchenko, T. S.; Della Longa, S.; Kotani, A.; Iwamoto, Y.; Bianconi, A. *Phys. Rev. B* **1994**, *50*, 5074−5080.

(51) Takahashi, Y.; Sakami, H.; Nomura, M. *Anal. Chim. Acta* **2002**, *468*, 345−354.

(52) Dai, Q.; Wang, X.; Chen, G.; Zheng, Y.; Lu, G. *Microporous Mesoporous Mater.* **2007**, *100*, 268−275.

(53) Van de Loosdrecht, J.; van der Kraan, A. M.; van Dillen, A. J.; Geus, J. W. *J. Catal.* **1997**, *170*, 217−226.

(54) Selvaraj, M.; Park, D. W.; Ha, C. S. *Microporous Mesoporous Mater.* **2011**, *138*, 94−101.

(55) Bradford, M. C. J.; Vannice, M. A. *J. Catal.* **1999**, *183*, 69−75.

(56) Wei, J.; Iglesia, E. *J. Catal.* **2004**, *224*, 370−383.

(57) David, B.; Uwe, R.; Frank, K.; Aimeryde, M.; Kai, C, S.; Herve, M.; Laurent, V.; Jean-Pierre, C.; Paul, B. W.; Chloe, T.; Christophe, C. *J. Catal.* **2013**, *297*, 27−34.

(58) Wang, S. B.; Lu, G. Q. M. *Appl. Catal., B* **1998**, *16*, 269−277.

(59) Nandini, A.; Pant, K. K.; Dhingra, S. C. *Appl. Catal., A* **2005**, *290*, 166−174.

(60) Yang, R.; Xing, C.; Lv, C.; Shi, L.; Tsubaki, N. *Appl. Catal., A* **2010**, *385*, 92−100.

(61) Ruckenstein, E.; Hu, Y. *Appl. Catal., A* **1997**, *154*, 185−205.

(62) Hou, Z.; Gao, J.; Guo, J.; Liang, D.; Lou, H.; Zheng, X. *J. Catal.* **2007**, *250*, 331−341.

(63) Trimm, D. L. *Sci. Eng.* **1977**, *16*, 155−189.

(64) Swaan, H. M.; Kroll, V. C. H.; Martin, G. A.; Mirodatos, C. *Catal. Today.* **1994**, *21*, 571−578.

(65) Tracz, E.; Scholz, R.; Borowiecki, T. *Appl. Catal.* **1990**, *66*, 133−147.

(66) Hu, Y. H.; Ruckenstein, E. *J. Catal.* **1999**, *184*, 298−302.

(67) Tsyganok, A. I.; Tsunoda, T.; Hamakawa, S.; Suzuki, K.; Takehira, K.; Hayakawa, T. *J. Catal.* **2003**, *213*, 191−203.

(68) Espinat, D.; Dexpert, H.; Freund, E.; Martino, G.; Couzi, M.; Lespade, P.; Cruege, F. *Appl. Catal.* **1985**, *16*, 343−354.

(69) Barros, E. B.; Demir, N. S.; Souza Filho, A. G.; Mendes Filho, J.; Jorio, A.; Dresselhaus, G.; Dresselhaus, M. S. *Phys. Rev. B* **2005**, *71*, 165422.

(70) Cuesta, A.; Dhamelincourt, P.; Laureyns, J.; Martínez-Alonso, A.; Tascón, J. M. D. *Carbon* **1994**, *32*, 1523−1532.

(71) Zhang, Z.; Verykios, X. E. *Catal. Today* **1994**, *21*, 589−595.

(72) Chen, Y.; Tomishige, K.; Fujimoto, K. *Appl. Catal., A* **1997**, *161*, L11−L17.

(73) Liu, D.; Quek, X.-Y.; Wah, H. H. A.; Zeng, G.; Li, Y.; Yang, Y. *Catal. Today* **2009**, *148*, 243−250.

(74) Tatsumi, T.; Koyano, K. A.; Tanaka, Y.; Nakata, S. *Chem. Lett.* **1997**, *5*, 469−470.

(75) Cassiers, K.; Linssen, T.; Mathieu, M.; Benjelloun, M.; Schrijnemakers, K.; Van Der Voort, P.; Cool, P.; Vansant, E. F. *Chem. Mater.* **2002**, *14*, 2317−2324.

(76) Matsumura, Y.; Nakamori, T. *Appl. Catal., A* **2004**, *258*, 107−114.

(77) Laosiripojana, N.; Sutthisripok, W.; Assabumrungrat, S. *Chem. Eng. J.* **2005**, *112*, 13−22.

(78) Campbell, C. T.; Peden, C. H. F. *Science* **2005**, *309*, 713−714.